ESAIM: Proceedings, Vol. 1, 1996, pp. 349–362
http://www.emath.fr/proc/Vol.1/

Application of 3D Particle Method to the Prediction of Aerodynamic Sound

K.P. Pothou, S.G. Voutsinas
NTUA, P.O. Box 64070
15710, Zografou
Athens, Greece

S.G. Huberson GEMH, Université du Havre, B.P. 540
76058 Le Havre cedex
France

O.M. Knio
Dept. of Mechanical Engineering
The Johns Hopkins University
Baltimore MD 21218, USA

Abstract

Low-Mach-number aeroacoustic theories are applied to predict far-field sound emission from vortex-dominated flows. The latter are simulated using three-dimensional vortex methods. Both particle schemes and filament-based schemes are used. Comparisons of model predictions with theoretical and experimental results on the interaction of two vortex rings are first discussed. Next, the schemes are used to examine the effect of initial conditions and 3D perturbations on the properties of the far-field acoustic pressure. Finally, a more elaborate wind-turbine model is presented and its application to the evaluation of several turbine-blade designs is summarized.

1 Governing equations and vortex sound theory

Noise is a small pressure perturbation related to the compressibility of fluids and its modelling must be based on the compressible Navier-Stokes equations. Although the full Navier-Stokes equations can be numerically solved, the complexity of the problem makes them very difficult to use in general. The main problems encountered are the derivation of noise-compatible external boundary conditions, and the usual need of very fine grids. In noise simulations, the problem is even more crucial since the grid is directly related to the lowest resolvable scale, and thus to the highest frequency which is accurately represented. An obvious way to overcome these difficulties is to introduce more physics in the problem in order to obtain a simplified formulation. This can be achieved by using a few more assumptions which are satisfied in most cases of audible noise.

We first assume that the noise sources are contained in a finite domain. In our case, the noise sources are mainly vorticity-generated pressure waves; thus, this assumption is equivalent to the requirement that the support of vorticity is compact. As a result, the flow field can be split into an inner and an outer domain, and the flow within the outer domain can be considered irrotational.

The second assumption is that the compressibility effects remain small enough so that the incompressible flow approximation holds for all but the acoustical part of the flow. The usual way to introduce this assumption is to consider that the Mach number, M, is low. If, in addition, density variations are small, this assumption will result in a decomposition of the problem into three sequential problems.

The low-Mach-number assumption is used together with the Helmholtz decomposition of the velocity field in order to obtain two different equations for the incompressible and compressible

part of the flow. The latter is assumed to be small enough to justify further linearization based on neglecting terms $O(M^2)$ and higher. This results in the two following problems: (a) the incompressible Navier-Stokes equations:

$$\frac{\partial \mathbf{U}}{\partial t} + (\mathbf{U} \cdot \boldsymbol{\nabla})\mathbf{U} + \frac{1}{\rho_o}\boldsymbol{\nabla} p_o = \nu \Delta \mathbf{U}$$

$$\boldsymbol{\nabla} \cdot \mathbf{U} = 0$$

where p_o and ρ_o denote the mean pressure and density of the fluid, respectively, and, (b) Lighthill's [8] acoustic pressure equation:

$$\frac{1}{c^2}\frac{\partial^2 p}{\partial t^2} = \Delta p + \frac{\partial^2 T_{ij}}{\partial x_i \partial x_j} \tag{1}$$

where

$$T_{ij} = \rho_o u_i u_j + (p_o - c^2 \rho_o)\delta_{ij}$$

Since the flow is considered isentropic, Lighthill's tensor T_{ij} becomes:

$$T_{ij} = \rho_o u_i u_j$$

In the inner domain, the Navier-Stokes equations can be replaced by the vorticity transport equation:

$$\frac{\partial \boldsymbol{\omega}}{\partial t} + (\mathbf{U} \cdot \boldsymbol{\nabla})\boldsymbol{\omega} = (\boldsymbol{\omega} \cdot \boldsymbol{\nabla})\mathbf{U} + \nu \Delta \boldsymbol{\omega} \tag{2}$$

Compressibility effects are present only in the acoustical part of the flow, i.e. the outer region. According to our assumptions, the flow field in the outer region is irrotational, and can therefore be described by means of a velocity potential. This suggests a domain decomposition of the flow.

From a numerical point of view, the far-field assumptions allow us to concentrate our computational resources in the inner region where sound is generated. In the outer domain, the computational effort is greatly reduced by the use of Lighthill's linear inhomogeneous wave equation.

However, imposition of adequate boundary conditions must be carefully addressed. Since we have a linear equation, an easy way to handle this problem is to rely on an integral formulation which implicitly satisfies the external boundary conditions. The most commonly-used integral representations are based on the linear relation between the acoustic pressure and the time derivative of the velocity potential. The latter can be expressed by means of an integral formulation using the vorticity field; thus, an integral representation of the pressure field based on the vorticity distribution is obtained.

Moreover, further simplification will be obtained by considering that the distance between the support of vorticity and the observation point is large. As a result, the integral representation for the far-field pressure will be written in a numerically tractable form. We first solve Lighthill's equation by using the Green's function of the wave equation,

$$\mathcal{G}(\mathbf{x}, t) = \frac{\rho_o}{4\pi}\frac{\delta(t - \tau - \frac{|\mathbf{x}-\mathbf{y}|}{c})}{|\mathbf{x} - \mathbf{y}|} = \frac{\rho_o}{4\pi}\frac{\delta(t_{ret})}{|\mathbf{x} - \mathbf{y}|}$$

Using this expression leads to the following integral representation for p:

$$p(\mathbf{x},t) = \frac{\rho_o}{4\pi}\int_\tau\int\int\int_{\mathcal{D}_\omega}\frac{\partial^2 v_i v_j}{\partial y_i \partial y_j}\frac{\delta(t_{ret})}{|\mathbf{x}-\mathbf{y}|}dyd\tau \tag{3}$$

The next step is to use an asymptotic method based on the previous assumptions that the characteristic length of the inner domain, l, is small compared to the acoustic wavelength, $\lambda = \mathcal{O}(l/\mathcal{M})$. As a result, $|\mathbf{x}|$ will be large compared to $|\mathbf{y}|$ in the integral and $|\mathbf{x}-\mathbf{y}|^{-1}$ can be approximated by $|\mathbf{x}|^{-1}$. Moreover, since $|\mathbf{x}| >> l$, we can use the following approximation:

$$\frac{\partial}{\partial x_i}f(t-\frac{|\mathbf{x}|}{c}) \simeq \frac{-x_i}{c|\mathbf{x}|}\frac{\partial}{\partial t}f(t-\frac{|\mathbf{x}|}{c})$$

Consequently, Eq. 3 takes the form:

$$p(\mathbf{x},t) = \frac{\rho_o}{4\pi c^2|\mathbf{x}|^3}\frac{\partial^2}{\partial t^2}\int\int\int_{\mathcal{D}_\omega}(\mathbf{x}\cdot\mathbf{y})\mathbf{x}\cdot(\boldsymbol{\omega}\times\mathbf{U})d\mathbf{y} \tag{4}$$

The main interest of the above approximation is that the time integral has been replaced by a time derivative which is an instantaneous quantity, thus easier to compute. Möhring [9] applied the far-field approximation to derive a simpler form of Eq. 4:

$$p(\mathbf{x},t) = \frac{-\rho_o}{12\pi}\frac{x_i x_j}{c_o^2 r^3}\frac{d^3}{dt^3}\mathcal{Q}_{ij}(t-\frac{r}{c_o})$$

where

$$\mathcal{Q}_{ij} = \int\int\int_{D_\omega} y_i(\mathbf{y}\times\boldsymbol{\omega})_j d^3y$$

is the second moment of vorticity.

2 Numerical methods

2.1 Vortex methods

The vortical part of the flow is simulated using either a vortex particle method [2] or a vortex filament method [6]. These methods have a strong common basis and differ primarily by the way the stretching term is accounted for. The vortex particle method simulates the following system:

$$\frac{\partial\boldsymbol{\omega}}{\partial t} + (\mathbf{U}\cdot\boldsymbol{\nabla})\boldsymbol{\omega} = (\boldsymbol{\omega}\cdot\boldsymbol{\nabla})\mathbf{U} + \nu\Delta\boldsymbol{\omega} \tag{5}$$

$$\mathbf{U}(\mathbf{x},t) = \frac{1}{4\pi}\int\int\int_{\mathcal{D}_\omega}\frac{\boldsymbol{\omega}(\mathbf{y},t)\times(\mathbf{x}-\mathbf{y})}{|\mathbf{x}-\mathbf{y}|^3}d\mathbf{y} \tag{6}$$

while application of the filament scheme is restricted to inviscid flows. On the other hand, both methods are based on the representation of the flow in terms of vorticity-carrying particles, specified by two vector quantities: the location and the amount of transported vorticity,

$$\mathbf{X}_i = \frac{\int_{P_i}\mathbf{x}dv}{\int_{P_i}dv}$$

$$\boldsymbol{\Omega}_i = \int_{P_i}\boldsymbol{\omega}dv$$

respectively. The velocity field is reconstructed from the discrete particle vorticities using a regularized version of the Biot-Savart integral, Eq. 6. A simple and convenient form is given by:

$$\mathbf{U}(\mathbf{x},t) = \frac{1}{4\pi}\sum_i \frac{\mathbf{\Omega}_i \times (\mathbf{x}-\mathbf{X}_i)}{(|\mathbf{x}-\mathbf{X}_i|^6+\epsilon^6)^{1/2}} \tag{7}$$

where ϵ is a small regularization parameter whose value has to be fixed with respect to the averaged distance between two particles. While many different forms of the regularized velocity field have demonstrated their ability to lead to accurate results, it is not yet clear whether one form has obvious advantages over others.

For brevity, we sketch the implementation of both schemes to simulation of the inviscid Helmholtz equation. In the particle representation, we rely on an integral formulation of the vortex stretching term, $(\boldsymbol{\omega}\cdot\boldsymbol{\nabla})\mathbf{U}$, which is obtained by straightforward differentiation of Eq. 5. This leads to the following set of ordinary differential equations for the vorticity and location of the particles:

$$\frac{d\mathbf{X}_i}{dt} = \mathbf{U}(\mathbf{X}_i,t)$$

$$\frac{d\mathbf{\Omega}_i}{dt} = \frac{3}{8\pi}\sum_j \frac{1}{|\mathbf{X}_i-\mathbf{X}_j|^5}[((\mathbf{X}_i-\mathbf{X}_j)\cdot\mathbf{\Omega}_i)((\mathbf{X}_i-\mathbf{X}_j)\wedge\mathbf{\Omega}_j) + (((\mathbf{X}_i-\mathbf{X}_j)\wedge\mathbf{\Omega}_j)\cdot\mathbf{\Omega}_i)(\mathbf{X}_i-\mathbf{X}_j)]$$

Application of the filament scheme is based on ordering Lagrangian particles along vortex tubes and using the circulation of the vortex tubes to characterize the vorticity of the elements. Thus, the particle vorticity is approximated by the product of the circulation of the vortex tube and the length of the material segment associated to the particle, i.e.

$$\mathbf{\Omega}_i(t) \simeq \Gamma\delta\mathbf{l}_i(t)$$

Using the above approximation, the velocity field is obtained again from (7). In addition, Kelvin's theorem is invoked to conclude that the circulation of vortex tubes remains unchanged while changes in the material length $\delta\mathbf{l}_i(t)$ are approximated from the deformation of the geometry of the vortex tube. Thus, direct simulation of the vorticity transport equation and evaluation of the stretching term are avoided, at the expense of small additional overhead associated with book-keeping of the geometry of tubes and computations of segment lengths [7].

2.2 Acoustic pressure computation

The main advantage of the domain decomposition method is that there is no feed back effect of the far-field flow on the vortex flow. The acoustic pressure can be computed after the incompressible calculations are completed, provided that sufficient information is stored. Using the particle discretization of the vorticity field, Eq. 4, the far-field acoustic pressure is approximated as:

$$p(\mathbf{x},t) = \frac{-\rho_o}{4\pi c^2|\mathbf{x}|^3}\frac{\partial^2}{\partial t^2}\sum_i (\mathbf{x}\cdot\mathbf{X}_i)\mathbf{x}\cdot(\mathbf{\Omega}_i\times\mathbf{U}_i)d\mathbf{y}$$

With the filament representation, Möhring's formula is used; it yields:

$$p(\mathbf{x},t) = \frac{\rho_o}{12\pi}\frac{x_i x_j}{c^2|\mathbf{x}|^3}\frac{d^3Q_{ij}}{dt^3}$$

where

$$Q_{ij} = \sum_m (\Gamma_m [\mathbf{X}_m]_i [\delta \mathbf{l}_m \times \mathbf{X}_m]_j)$$

The time derivatives in the above equations are estimated using finite-difference schemes.

3 Interaction between two vortex rings

In this section, we consider the flow generated by two interacting coaxial vortex rings. The initial configuration is illustrated in Fig. 1. When their circulations have identical signs, the motion of the two vortex rings is periodic, with each vortex ring passing through the other during one period. This will be referred to as the mutual threading problem. When the ciculations are of opposite sign, the vortex rings undergo a head-on collision and the flow maintains its symmetry. Both problems have been studied by Kambe [4, 5] who gave theoretical as well as experimental sound predictions, thus providing good test cases for our aeroacoustic model.

3.1 Mutual threading

The mutual threading of two vortex rings may be summarized as follows. The two rings have the same circulation and their induced velocity field is such that the speed of the rear vortex is larger than that of the front one. As a result, the radius of the trailing vortex ring becomes smaller and threads through the leading vortex. Consequently, the axial position of the two vortices is inversed and a periodic motion is established. Below, results of our simulations are compared with the theoretical predictions of Kambe.

In Fig. 2 the ring radius is shown against the distance between the two vortex rings for three different initial separations. Each of the three curves represents the position of the front vortex ring during a complete turn. The time needed to complete one turns defines the period T, which is used to normalize time. The evolution of the separation distance between the two rings is plotted in Fig. 3. The translational speed of the mean axial position of the two rings is non-uniform (Fig. 4). The observed frequency is twice the frequency of the separation of the rings. There are small differences between our results and those of Kambe. They are probably due to numerical errors as well as to errors in recovering Kambe's curves.

The sound emitted by this interaction is associated with the non-uniformity of the axial motion of the rings. The evolution of the third time derivative of Q_{ij} is given in Fig. 5. It has the same frequency as the speed of the mean axial position and depends strongly on the initial separation of the rings. The peak values of our results are higher than those of Kambe. This is due to the difference observed between the predictions of the speed of the mean axial position as shown in Fig. 4. Experimental data are not available but the agreement with the theoretical analysis of Kambe is good, giving confidence in the numerical model.

3.2 Head-on collision

During the collision process, a deceleration in the motion of the two vortex rings occurs as the rings begin to approach each other. Meanwhile, their radii increase rapidly. Computed results are presented for the following conditions, which coincide with the experimental conditions of Kambe [5]: Initial vortex ring radius $R = 0.0054$m, initial translation velocity $U = 57$m/s, observer's distance $|\mathbf{x}| = 0.5$ m.

Figure 6 shows computed pressure profiles together with experimental data obtained by Kambe [4]. Also shown are inviscid calculations of Kambe based on asymptotic approximations and the calculations that he obtained by means of a viscous correction. The favorable agreement between our predictions and Kambe's measurements [4] shows that the numerical model reproduces the basic features of sound emission. The quantitative agreement between computed predictions and experimental data should be emphasized, especially since vortex methods are generally expected to over-predict sound levels.

Further examination of Fig. 6 shows that results of the present model lie between Kambe's inviscid and viscous curves. This suggests that there may be need for improving the modelling of diffusion effects in the simulations. However, Kambe mentions that an adjusting parameter must be added so as to get a good fit with the observations. This indicates that diffusion is coupled to internal motions within the core of the vortex ring and an efficient model should include an accurate description of the core structure evolution.

The role of the core structure can be examined by comparing acoustic pressure predictions obtained by fixing the initial core structure and varying the initial distance d (Fig. 7). At early stages, the necessary adaptation of the initial conditions results in oscillations which are similar for all the cases considered. Later on, as the rings are approaching each other, this similarity vanishes, indicating that the small differences observed in the early stages are now growing due to strong interactions between the two vortex rings. Moreover, this can not be corrected by a simple rescaling of time. This indicates that the problem is very sensitive to initial conditions which, at the experimental level, can not be accurately known.

3.3 Non-axisymmetric collisions

Additional insight into the role of core structure variation is gained by considering the impact of: (a) short-wave unstable perturbations and (b) long-wave perturbations with characteristic wavelength much larger than the vortex core. Figure 8 shows the evolution of one of the 3D rings during the collision process. At the start of the computation, the rings are perturbed (from an otherwise axisymmetric state) at the most unstable azimuthal bending mode [11, 6]. For the present conditions, 12 sinewaves of small amplitude are used. The simulation is performed using a filament-based scheme which maintains the 12-fold azimuthal symmetry of the initial configuration in order to speed up the computations. A comparison between axisymmetric and 3D far-field sound predictions is made in Fig. 9. In both axisymmetric and 3D computations, a fixed quadrupolar far-field directivity is obtained while, as shown in Fig. 9, very small differences in acoustic pressure levels are detected. The small impact of unstable bending waves on far-field sound emission may be explained by verifying that the absolutely unstable growth of the waves has very little impact on the time evolution of second moments of vorticity and, consequently, on far-field sound.

The computations above are finally contrasted with results for slender rings perturbed using long waves. Fig. 10 shows the evolution of a thin vortex ring at early stages of a head-on collision evolution event. The two vortex rings are initially perturbed using small-amplitude helical waves with wavenumbers 1 and 2. Note that, in the present case, the perturbation waves travel around the circumference of the ring without significant change in their form or amplitudes. Nonetheless, as shown in Fig. 11, the evolution of the waves has strong impact on far-field sound emission. In particular, it leads to significant departures from axisymmetric computations which, at similar stages in the collision, essentially predict zero far-field acoustic pressure. Also note that, while still quadrupolar in nature, the directivity of the far-field pressure distribution is no longer time-independent. These results amplify our earlier observation that accurate predictions of far-field noise should include adequate representation of the relevant modes of large-scale vortex motion as

well as internal core structure variation.

4 Example of a complex problem: wind turbine noise

4.1 Wind turbine flow

A wind turbine is made of three distinct parts: a rotor, a nacelle which hosts the electromechanical device, and a tower. From an aerodynamic point of view, in the flow around a wind turbine we can distinguish three regions: (a) the wake region, which extends downstream of the turbine and contains the vorticity which is shed from the blades and the tower, (b) the rotor region, which contains the blades and the tower, and (c) the solid surface region corresponding to the turbulent boundary layers which develop over the blades and the tower. The lowest scales of motion are those of the third region, and a direct description of the flow using the same model for the whole flow field domain would be impossible. One way to deal with this problem is to adopt different methods suitable to describe the flow in the three different regions.

The model used herein is based on an inviscid flow approximation which restricts the impact of viscous effects along separation lines on the tower and the blade wherefrom vorticity is released in the free-flow. The boundary layer is assumed to remain attached elsewhere, and the flow due to the presence of solid-walls is described with lifting surface models.

The wake region is discretized by means of vortex-carrying particles according to the method described in Section 3. Finally the wind inflow is assumed to be frozen, i.e. the impact of the wind turbine and its wake on the external vortical flow is neglected. The model has been extensively validated for wind turbines [10]; sample results for a wind turbine showing the computational particles in its wake are provided in Fig. 12.

4.2 Sound generation: A "noisy" line model

Sound generated by wind turbines is not limited to low-frequency vortex noise. The main noise source is due to the turbulent flow fluctuations developed over the blades. So an accurate description of the relevant phenomena would require computation of the compressible viscous turbulent flow around the blades. It has been previously mentioned that such a computation is impossible, and that a rough model has to be introduced. In this work, the characteristics of noise sources within boundary layers are related to the vortical flow by means of empirical laws. Based on the 3D inviscid calculations the overall flow characteristics over the blades and tower are determined (effective angle of attack, reference velocity, etc.). Next these data are used as input in 2D boundary layer calculations. Finally the boundary layer characteristics resulting from these computations are correlated (through appropriate scaling) to the empirical expressions which Brooks et al. [1] obtained by fitting with wind tunnel measurements. The results are then incorporated into the model by introducing sources along the blade in a similar fashion to the well-known lifting line model in which the aerodynamic forces are replaced with noise generators.

This model was used to predict the noise generated by a wind turbine equipped with rotors having changeable blade tips. The aim of that work was to evaluate different blade designs and complement to experimental measurements. Comparison between numerical and experimental results was favorable. A sample of the results is presented in Fig. 13. In all cases, the trends observed in measurements were recovered by the simulations [3]. In particular, experimental and numerical results predicted the same most-silent blade design.

5 Conclusion

In the present paper some of the questions related to the computation of vortex sound have been considered at different levels of complexity. Vortex particle and vortex filament approximations have been used to devise numerical methodologies which enable the study of low-Mach number noise emissions from two interacting vortex rings. The results obtained are considered encouraging since, on one hand, they clearly show the significant capabilities of vortex methods in analyzing vortex sound, and, on the other, they highlight areas which need improvement in the models. Of particular importance are the remarks concerning core structure evolution, which is found to play a significant role when vortex interactions are intense.

At the level of engineering applications, the model was extended to include also high frequency noise sources originating from turbulence. Application to the case of a wind turbine confirmed that in spite of the simplifications, consistent predictions can be obtained which can guide the correct design of wind turbine blades.

Acknowledgments

The authors wish to acknowledge helpful discussions with Prof. D. Juvé. Some computations were performed at the Pittsburgh Supercomputer Center.

References

[1] Brooks, T.F., Pope, D.S. and Marcolini, M.A., Airfoil Self Noise and Prediction, NASA Reference Publication 1218, 1989.

[2] Choquin, J.P. and S. Huberson, S., "Interaction Between Numerical and Physical Instabilities in Vortex Flows," *Int'l. J. Num. Meth. Fluids*, **11**, pp. 541–553.

[3] Huberson, S., Pothou, K.P. and Voutsinas, S.G., Wind Turbine Noise: Recent Developments of a Vortex Type Aeroacoustic Numerical Tool, EWEC'94, Thessaloniki, 1994.

[4] Kambe, T., "Acoustic Emission by Vortex Motions," *J. Fluid Mech.*, **173**, pp. 643–666, 1986.

[5] Kambe, T. and Minota, T., "Acoustic Wave Radiated by Head-on-Collision of Two Vortex Rings,", *Proc. Roy. Soc. London*, **A386**, pp. 277–308, 1983.

[6] Knio, O.M. and Ghoniem, A.F., "Numerical Study of a Three-Dimensional Vortex Method," *J. Comp. Phys.*, **86**, pp. 75–106, 1990.

[7] Leonard, A., "Computing Three-Dimensional Incompressible Flows with Vortex Filaments," *Ann. Rev. Fluid Mech.*, **17**, pp. 523–559, 1985.

[8] Lighthill, M.J., "On Sound Generated Aerodynamically I. General Theory," *Proc. Roy. Soc. London*, **222A (1107)**, pp. 564–587, 1952.

[9] Möhring, W., "On Vortex Sound at low Mach Number," *J. Fluid Mech.*, **85**, pp. 685–691, 1978.

[10] Voutsinas, S.G., Belessis, M. and Huberson, S., Dynamic Inflow Effects and Vortex Particle Methods, ECWEC'93, Travemunde, 1993.

[11] Widnall, S.E. and Tsai, C.-Y., "The Instability of the Thin Vortex Ring of Constant Vorticity," *Proc. Roy. Soc. London*, **287 (A1334)**, pp. 273–305, 1977.

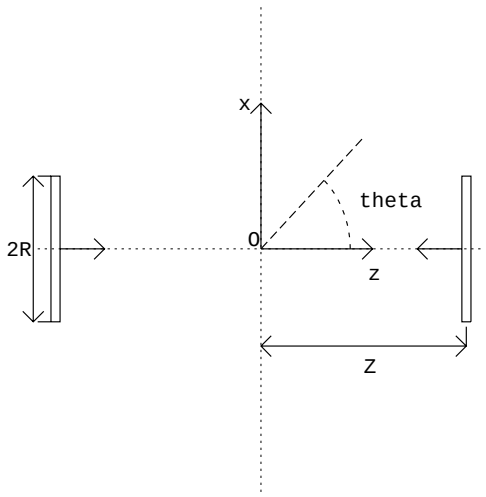

Figure 1: Initial conditions for the problem of two interacting vortex rings.

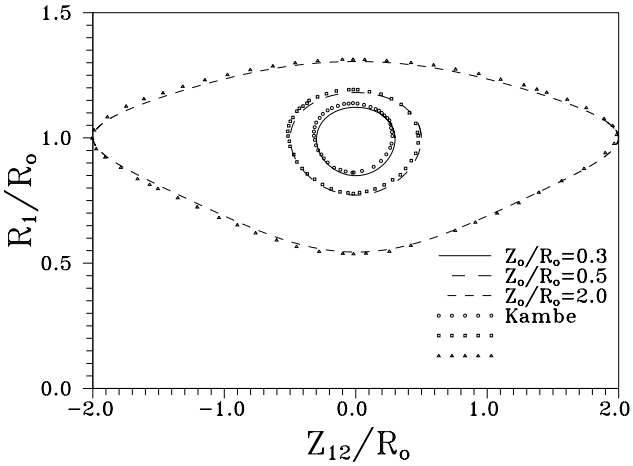

Figure 2: Ring radius evolution against the distance between the two vortex rings. Z_{12} is the distance between the two rings and R_1 is the first ring radius. R_0 is the radius of both rings at time $t = 0$.

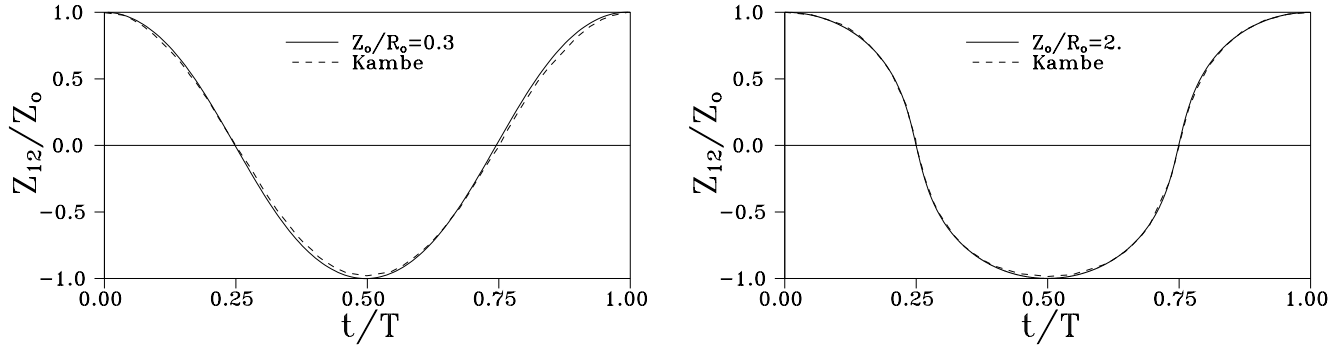

Figure 3: Evolution of the separation distance between the two rings. Z_{12} is the distance between the two rings. R_0 is the radius of both rings at time $t = 0$.

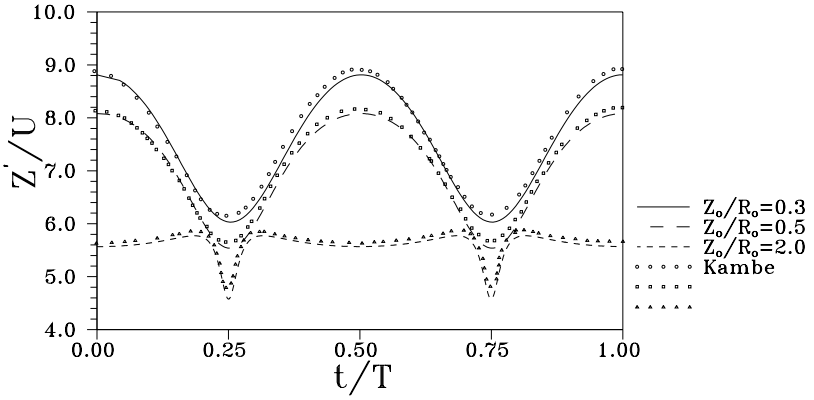

Figure 4: Translational speed Z' of the mean axial position of the two rings.

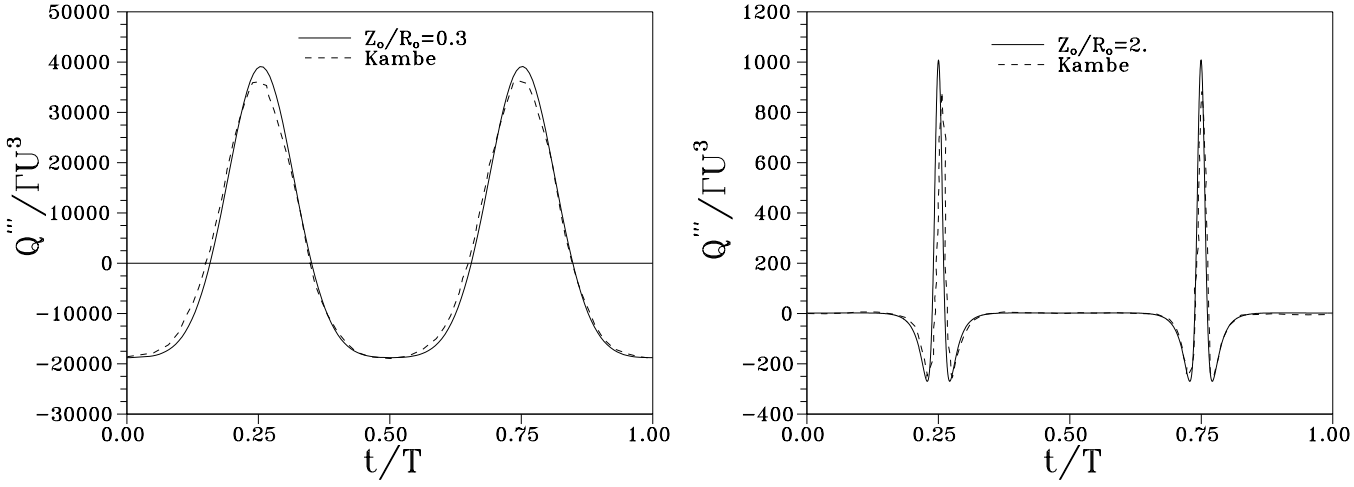

Figure 5: Evolution of the third time derivative of Q_{ij} is given versus time.

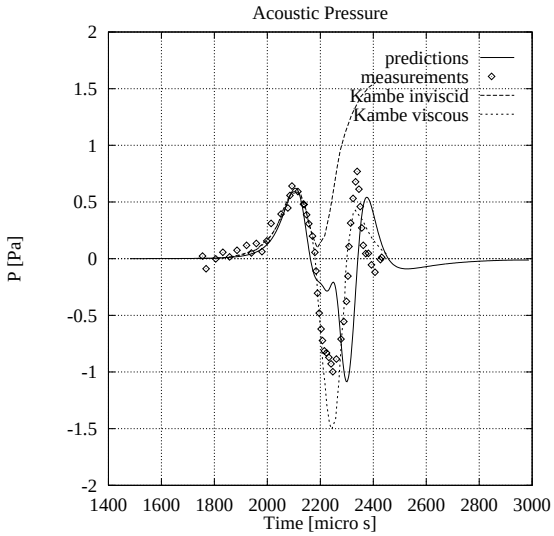

Figure 6: Computed pressure profiles together with experimental data obtained by Kambe [4].

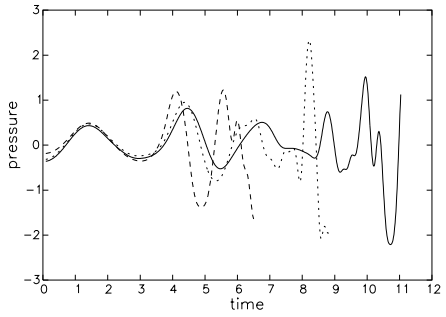

Figure 7: Acoustic pressure signals obtained using a deformable core model and different initial separation distance, $d/R = 4$ (solid), $d/R = 3$ (short dash), and $d/R = 2$ (long dash).

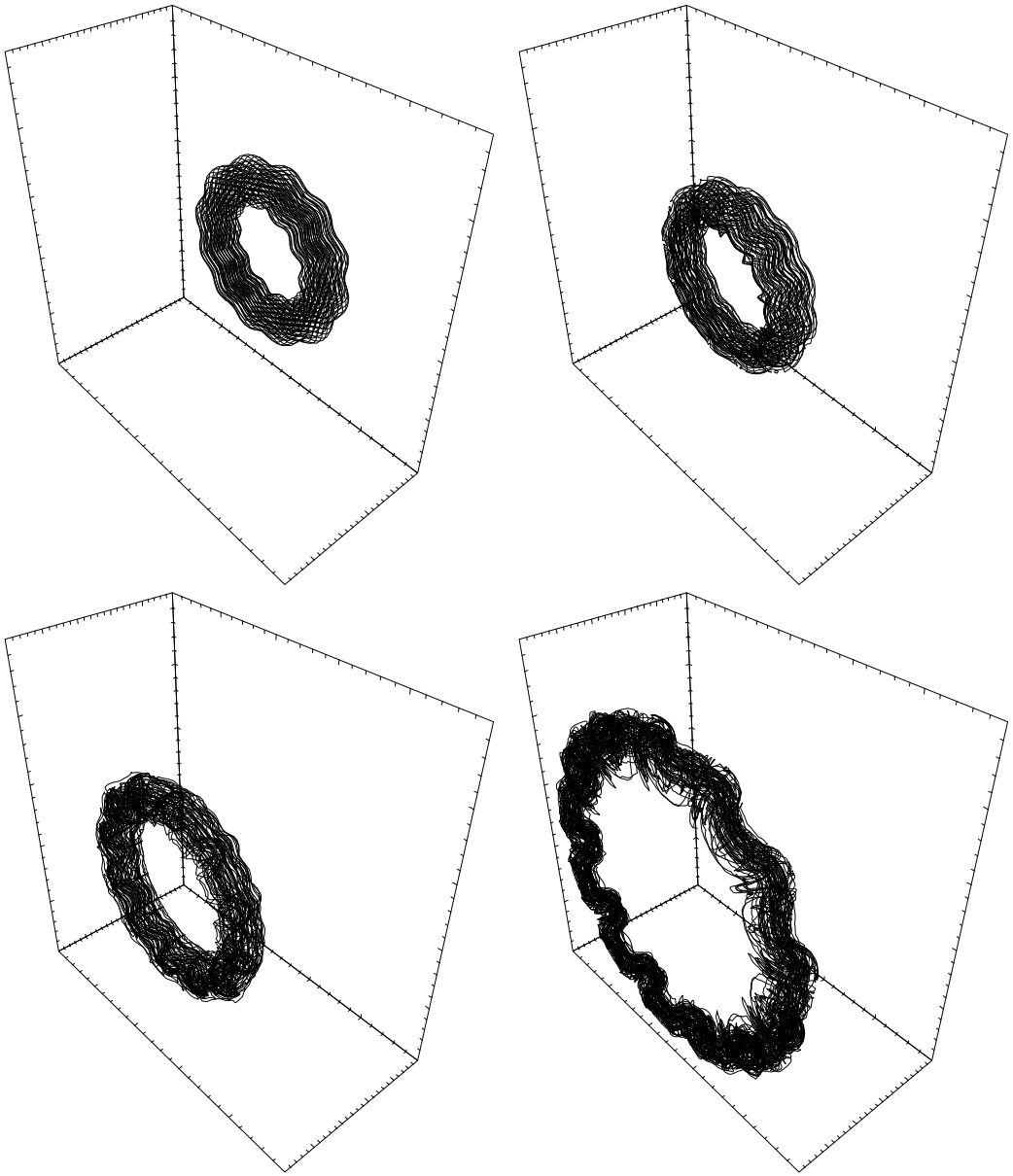

Figure 8: Evolution of one of the 3D rings during the collision process.

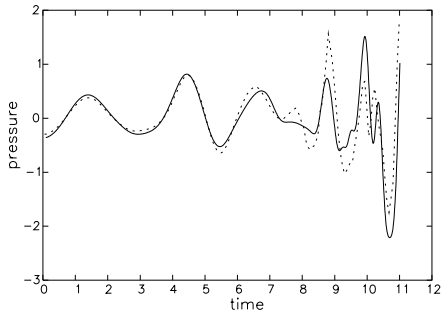

Figure 9: Comparison between axisymmetric (continuous) and 3D (dotted) far-field sound predictions.

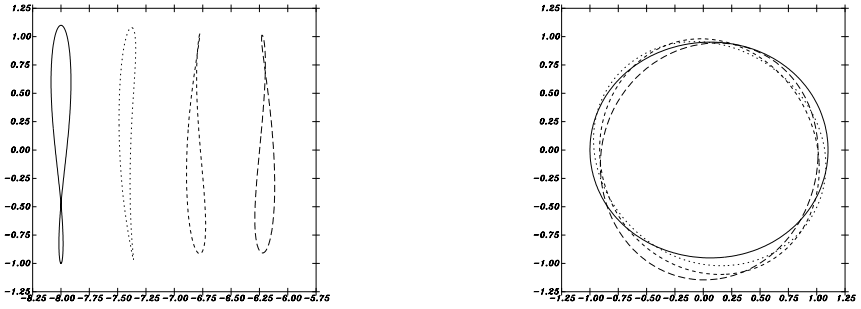

Figure 10: Evolution of a thin ring at early stages of a head-on collision. The plots show projections of the ring centerline on an azimuthal plane (left) and a streamwise plane (right) at different times.

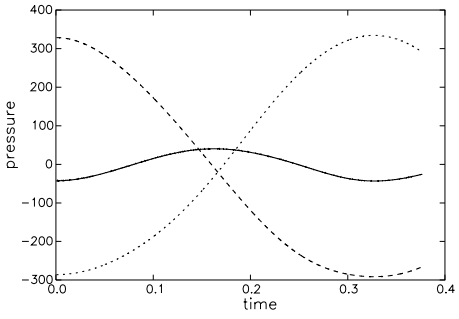

Figure 11: Evolution of the far-field acoustic pressure during the early stages of collision between perturbed slender vortex rings. The solid line depicts emission along the axis of propagation of the ring, while the dashed lines show emission along two orthogonal directions in a streamwise plane.

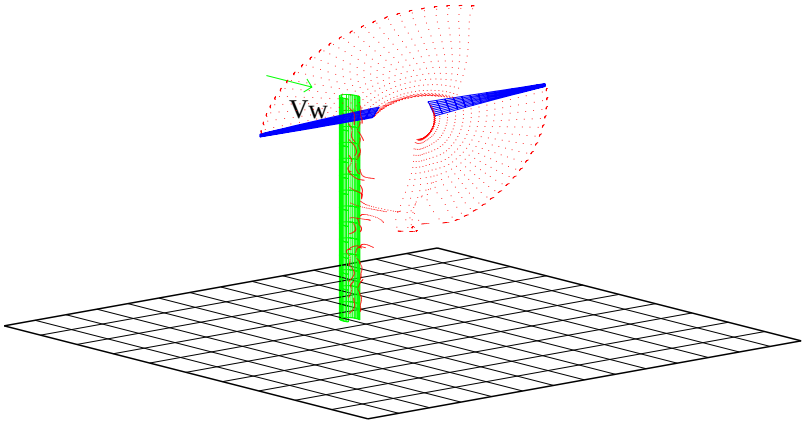

Figure 12: Computational particles in the wake of a wind turbine.

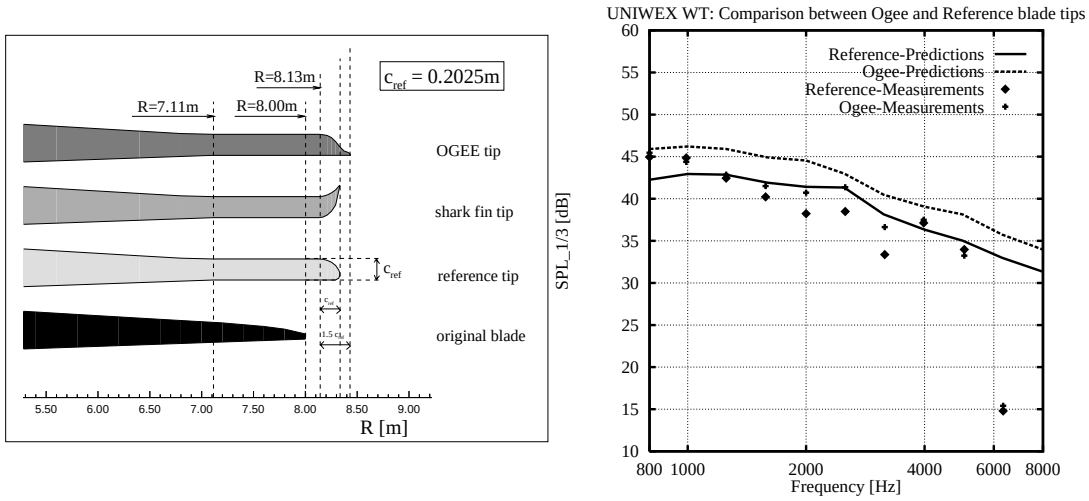

Figure 13: (left) Different blade tip shape. Only the Ogee and reference tip have been used in the present calculations. (right) Experimental and numerical pressure for different blade designs.